Supporting information

Calculation of Agari model

The formation of a continuous filler network structure is key to achieving high TC in composite.[1] The Agari model, which is widely used to evaluate the thermal conductivity (TC) of polymer-based composites, is adopted to theoretically analyze the influence of the constructed 3D EG network on TC. The equation is given by

$$\log k = \varphi C_2 \log k_f + (1-\varphi)\log (C_1 k_m) \quad (1)$$

where k, k_f and k_m stand for the TC of the composites, EG filler and neat epoxy, respectively, and φ is the volume fraction of EG. C_1 is a coefficient reflecting the influence of EG on the crystallization behavior of the epoxy matrix. Referring to the previous reports, the value of C_1 is determined as 1 here. C_2 is a parameter representing the ability of the fillers to form thermal conduction channels, and generally in the range of 0-1. The higher value of C_2 corresponds to the greater the ability for the EG to form thermally conductive paths.[2, 3] The predicted TC values of the Agari model are calculated by setting C_2 as 1.

Finite element simulation modeling

Modeling software Spaceclaim was used to establish the three coatings model. The scale of the models were all 2 cm × 2 cm × 1 mm and the thickness of each coating was set up to 200 μm. After modeling, the models were imported to COMSOL simulation software. The grid area was divided using the meshing function of COMSOL, and the material properties was set according to the database in simulation

software or measured value in experiment. In the configuration, the initial temperature of the coating is set to 80 ℃. The total simulation time was 4000 s and the convective heat transfer of the model remains consistent. The diameter of the air domain was set up to 4 cm. The mesh discretization was physics-controlled without manual intervention. The heat transfer simulation assumed a default system temperature of 20 °C (ambient), with identical convective heat transfer parameters maintained across all three models.

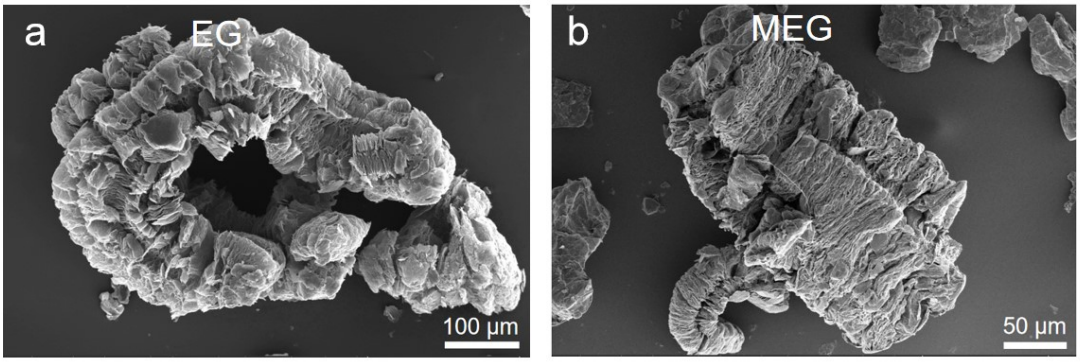

Fig. S1. SEM image of (a) EG and (b) MEG.

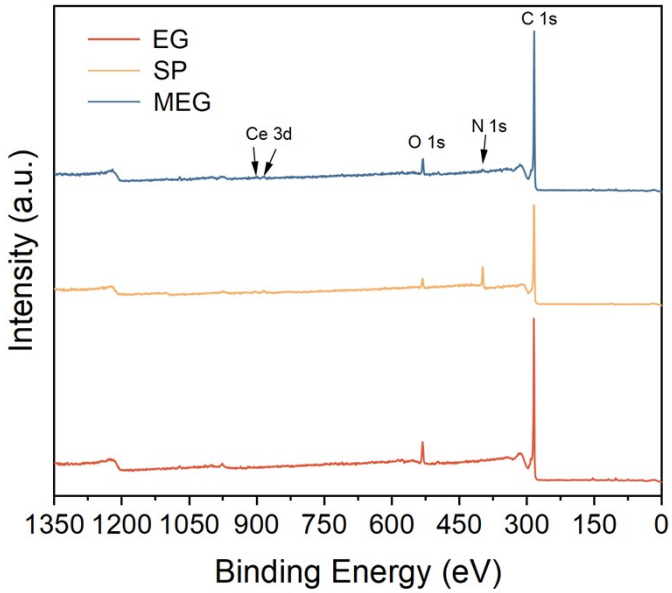

Fig. S2. XPS of EG, SP and MEG.

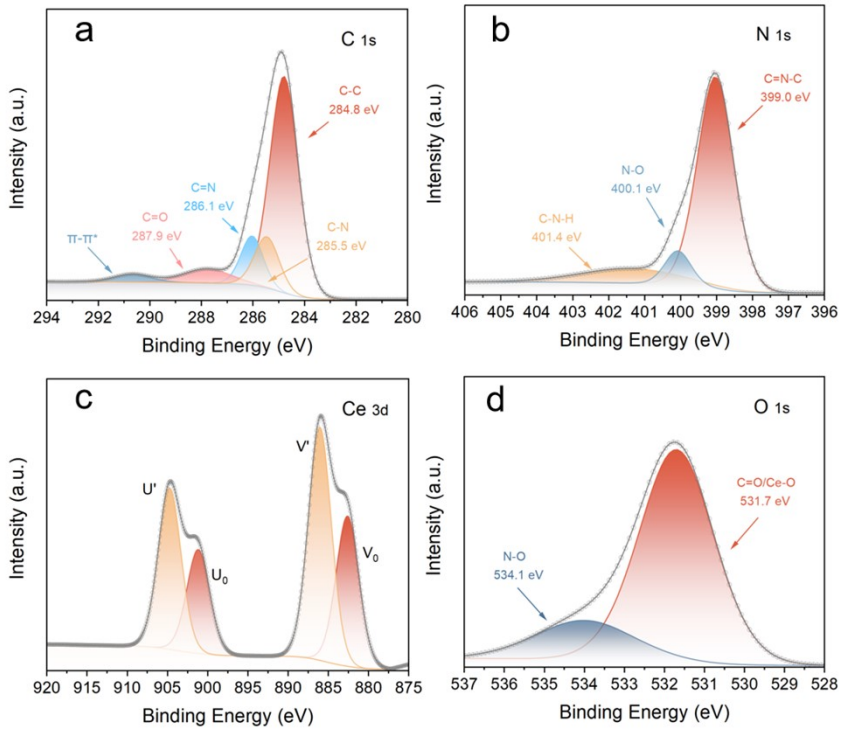

Fig. S3. High-resolution spectra of SP: (a) C 1s, (b) N 1s, (c) Ce 3d and (d) O 1s.

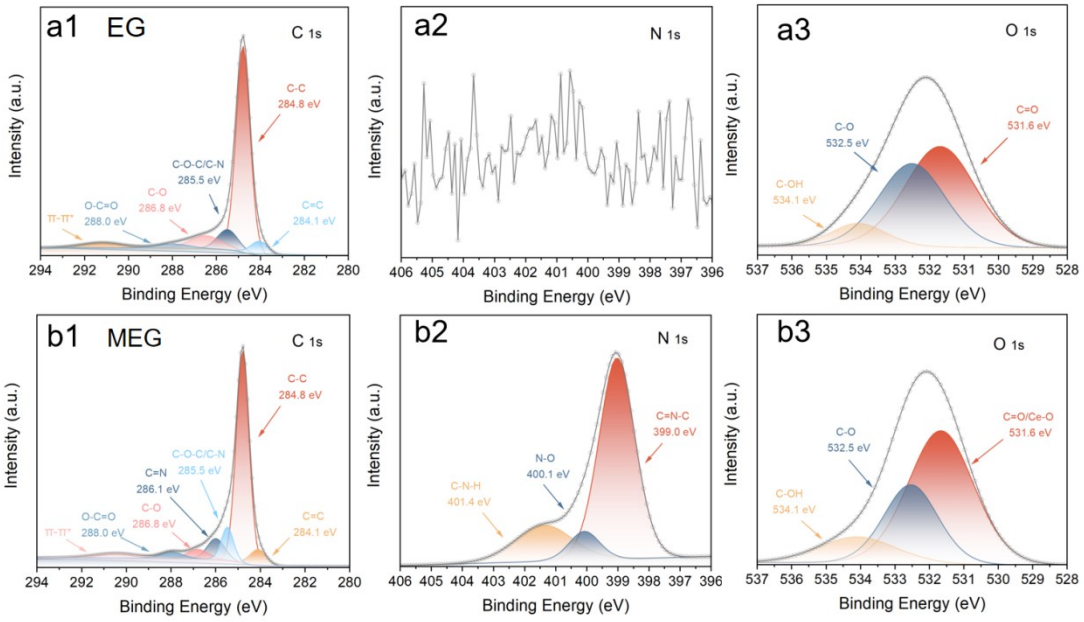

Fig. S4. High-resolution spectra of EG: (a1) C 1s, (a2) N 1s, (a3) O 1s and MEG: (b1) C 1s, (b2) N 1s, (b3) O 1s.

Component analysis of EG, SP and MEG

For analyzing the surface chemical composition of SP **(Figure S3)**, EG **(Figure S4a1-a3** and **Figure 2d)**, and MEG **(Figure S4b1-b3** and **Figure 2h)**, XPS was carried out to detect the three samples. As can be seen in **Figure S3a**, the C 1s peak at 284.8, 285.5, 286.1, 287.9, and 290.7 eV can be attributed to C-C, C-N, C=N, C=O, and π-π* interaction, respectively.[4-6] High-resolution spectra of N 1s in SP (**Figure S3b**) exhibits three peaks at 399.0, 400.1 and 401.4 eV can attribute to C=N-C, N-O, and C-N-H, respectively. In **Figure S3c**, the bands labeled "v" and "u" correspond to the $3d_{5/2}$ ionization and $3d_{3/2}$ ionization, respectively. Ce^{4+} ions are associated with peaks labeled u, v, u", v", u"', v"', while Ce^{3+} ions are associated with peaks labeled u_0, v_0, u', v'.[7, 8] As can be seen, it is clear that the high-resolution spectra of Ce 3d for SP only show the peaks (u_0, v_0, u', v') associated with Ce^{3+} ions, indicating that all the cerium ions in the synthesized SP exist in the trivalent state. As shown in **Figure S2**, the total spectral pattern of MEG exhibits the peak of C, N, O, and Ce. Compared to EG (**Figure S4a1**), high-resolution spectra of C 1s in MEG appear C=N bond at 286.1 eV (**Figure S4b1**), which can be attributed to SP-modified EG. Moreover, other peaks at 284.1, 284.8, 285.5, 286.8, 288.0 and about 291.0 eV can be attributed to C=C, C-C, C-N/C-O-C, C=O, O-C=O, and π-π* interaction, respectively. As can be seen in **Figure S4a2** and **Figure S4b2**, there is no apparent and N 1s peak in EG**.** In addition, high-resolution spectra of N 1s in MEG exhibits three peaks at 399.0, 400.1, and 401.4 eV can attribute to C=N-C, N-O, and C-N-H[9, 10], respectively, which is consistent with the spectra of SP. The high-resolution spectra of O 1s were shown in **Figure S4a3** and **Figure S4b3**. On the whole, EG is successfully modified by SP.

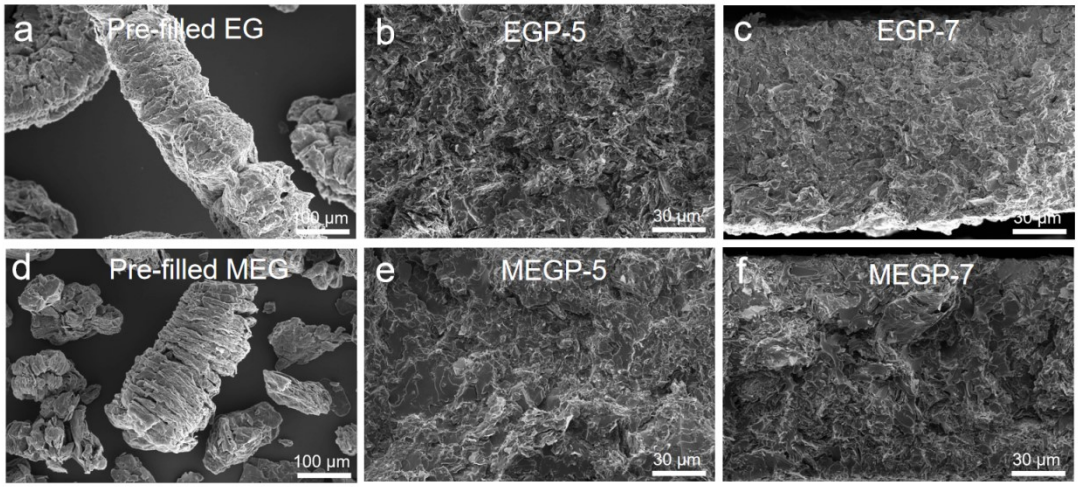

Fig. S5. SEM image of (a) pre-filled EG, (b) EGP-5 coating, (c) EGP-7 coating, (d) pre-filled MEG, (e) MEGP-5 coating and (f) MEGP-7 coating.

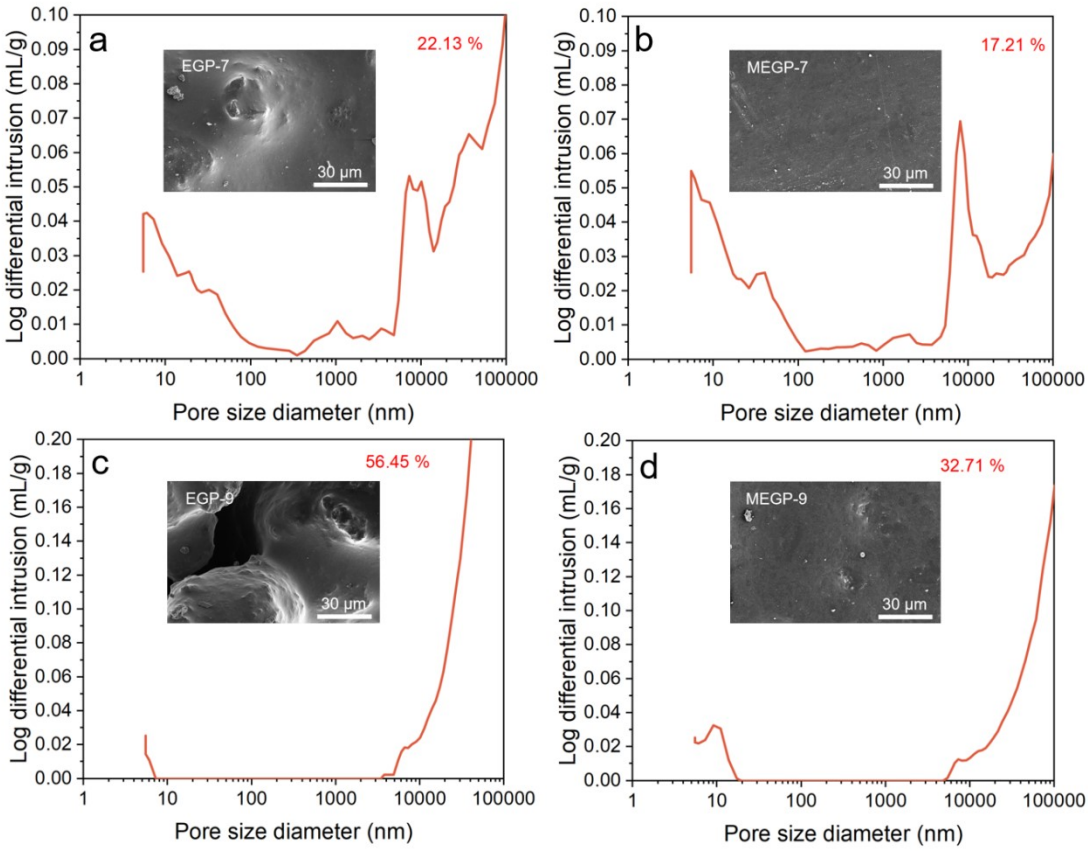

Fig. S6. Surface SEM image and porosity of (a) EGP-7, (b) MEGP-7, (c) EGP-9 and (d) MEGP-9 coatings.

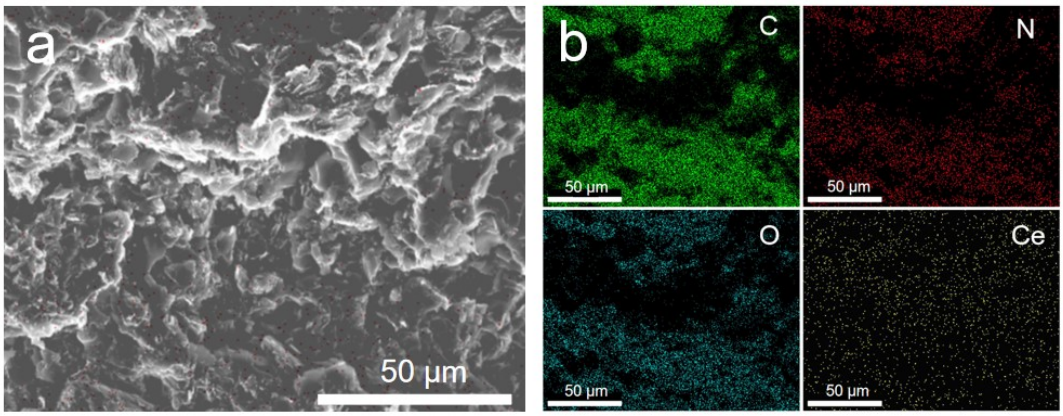

Fig. S7. SEM (a) and EDS (b) image of the MEGP-7 coatings section.

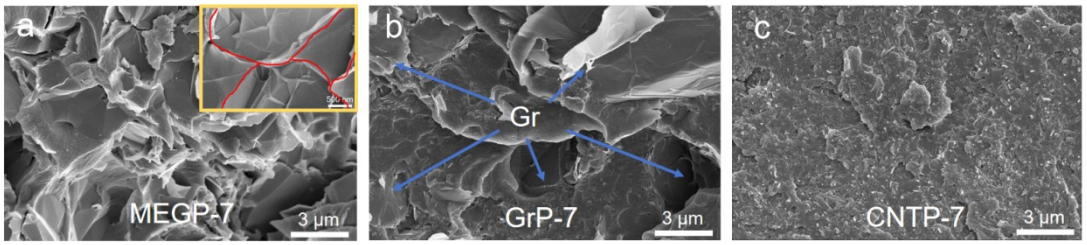

Fig. S8. Microstructure SEM image of (a) MEGP-7, (b) GrP-7 and (c) CNTP-7.

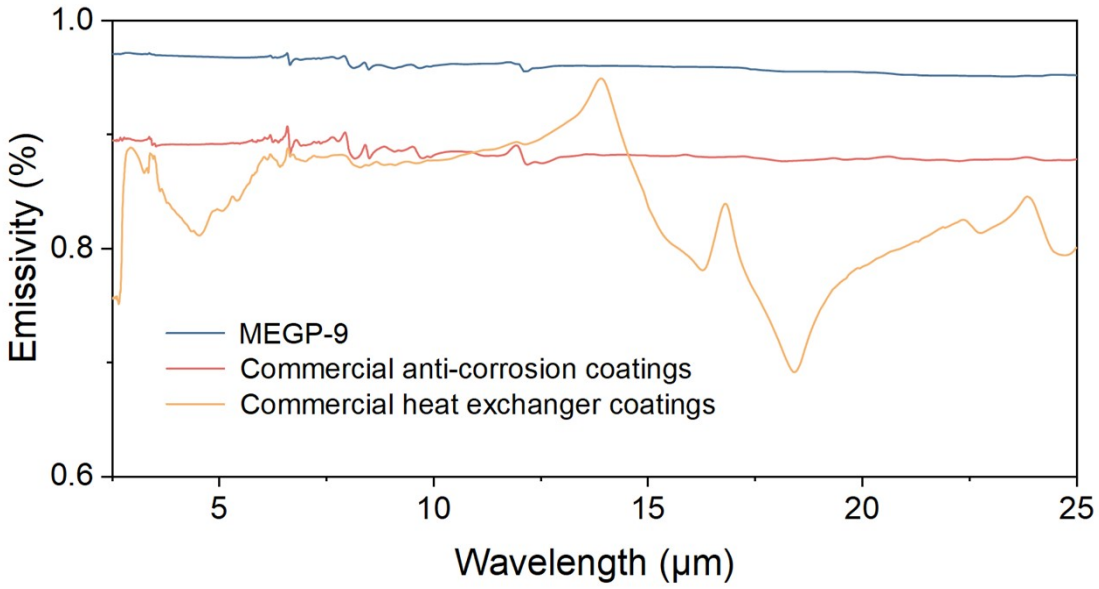

Fig. S9. The infrared emissivity of the MEGP-9, commercial anti-corrosion coating and commercial heat exchanger coating.

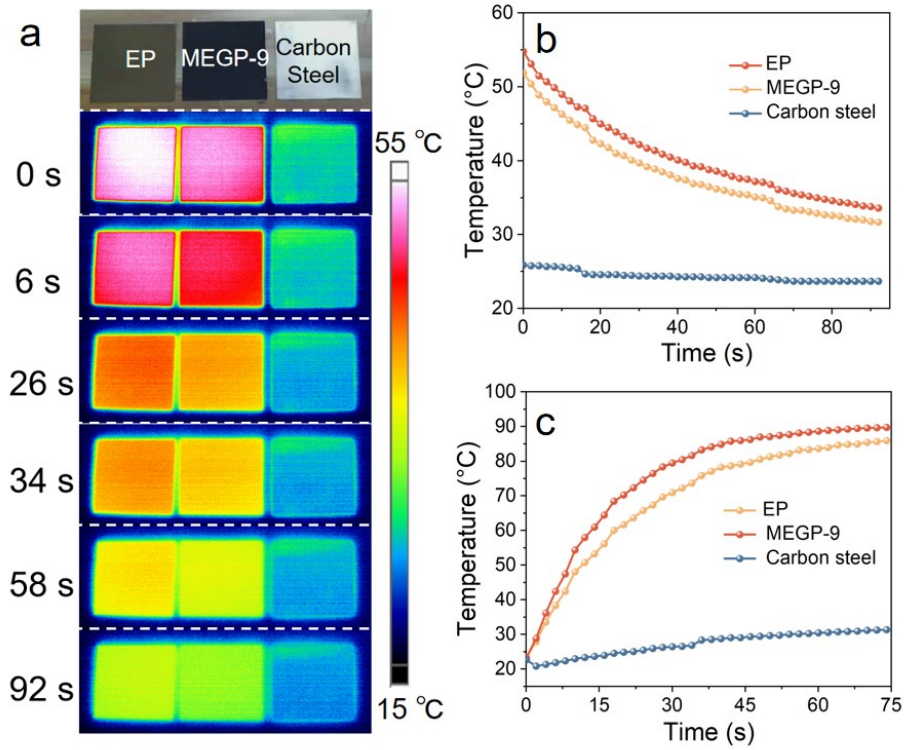

Fig. S10. Heat transfer performance of the coatings: the cooling/heating test image and temperature change curve of EP, carbon steel and MEGP-9 coatings.

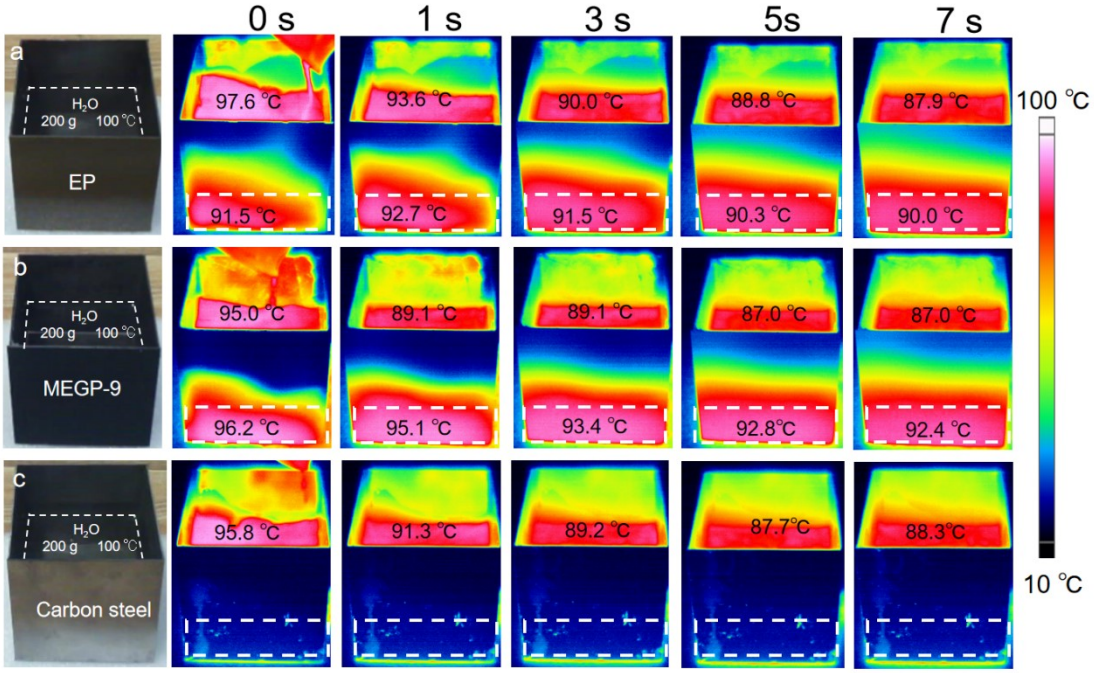

Fig. S11. Boiling water cooling experiment and infrared thermography images of EP, carbon steel and MEGP-9 coatings.

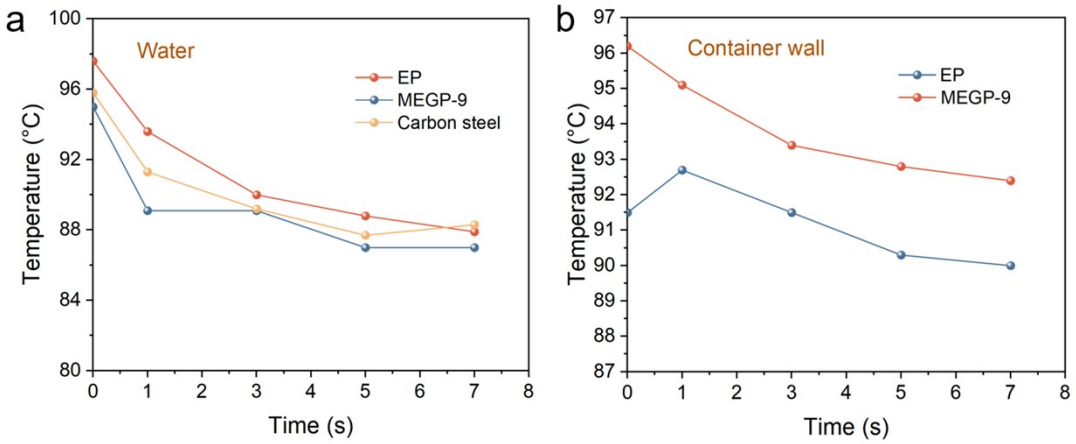

Fig. S12. Temperature change curve of water and container wall.

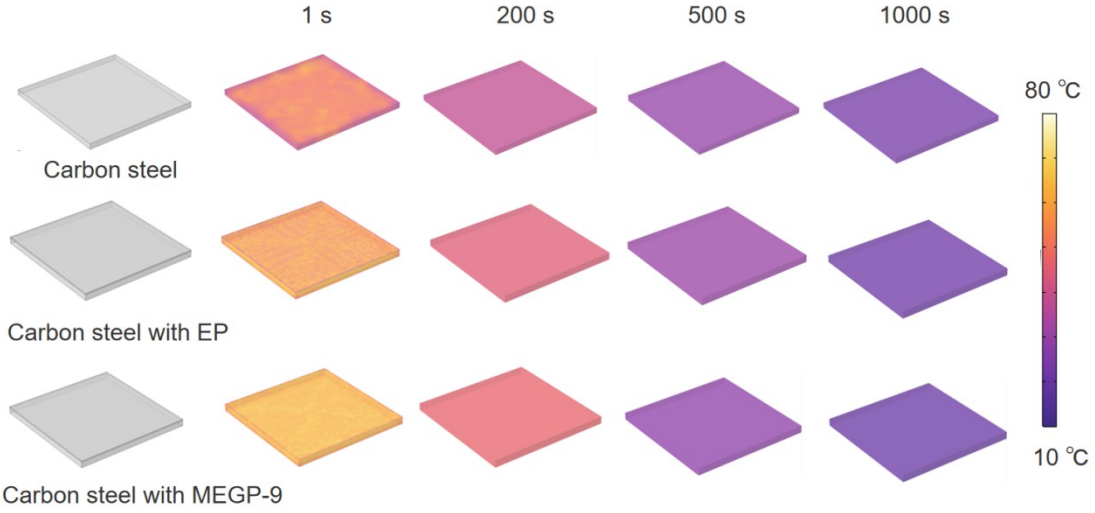

Fig. S13. Finite element simulation of cooling test with EP, carbon steel and MEGP-9 coatings.

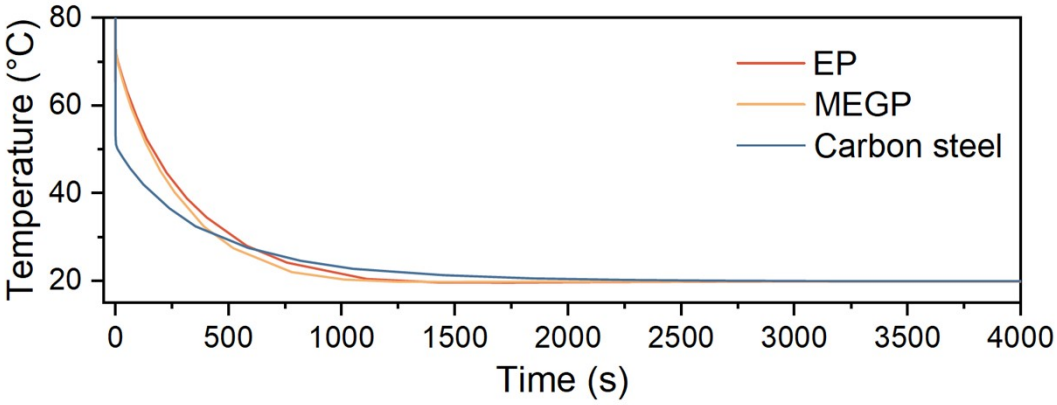

Fig. S14. Surface temperature of EP, carbon steel and MEGP-9 coatings in finite element simulation.

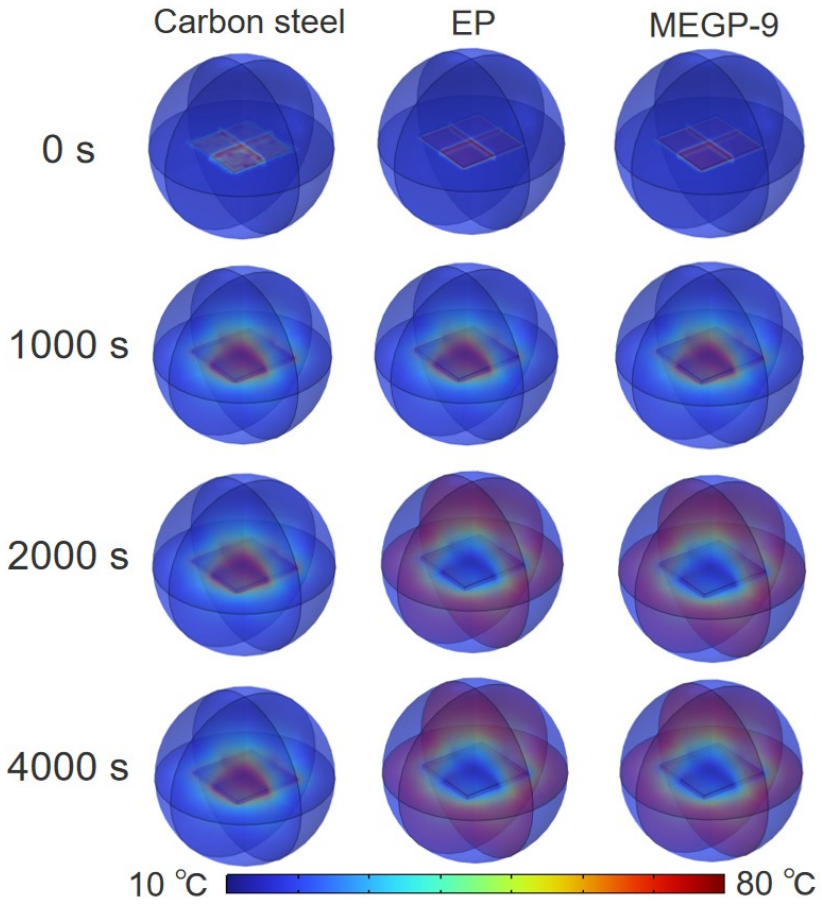

Fig. S15. Air domain heat transfer of EP, carbon steel and MEGP-9 coatings.

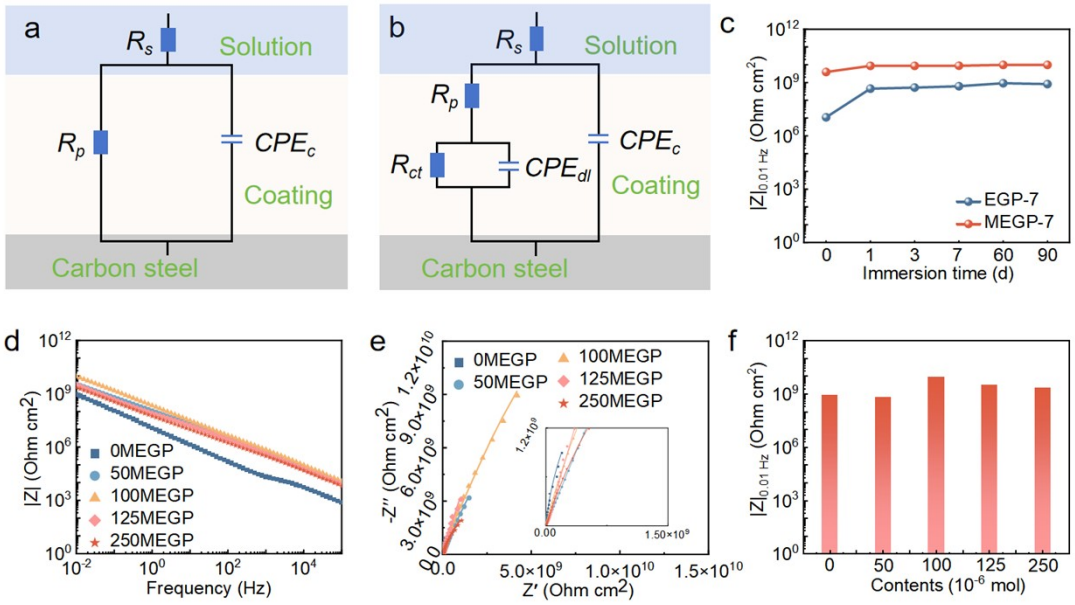

Fig. S16. The equivalent circuit models used to fit the EIS data (a-b), where R_s, R_p and R_{ct} refer to the solution resistance, the coating resistance and the charge transfer resistance, respectively. CPE_c and CPE_{dl} represent the coating constant phase element and the electrical double layer constant phase element. EIS curves of MEGP coatings with different contents of Schiff base-Ce complex immersion in 3.5% NaCl aqueous solution (c-f).

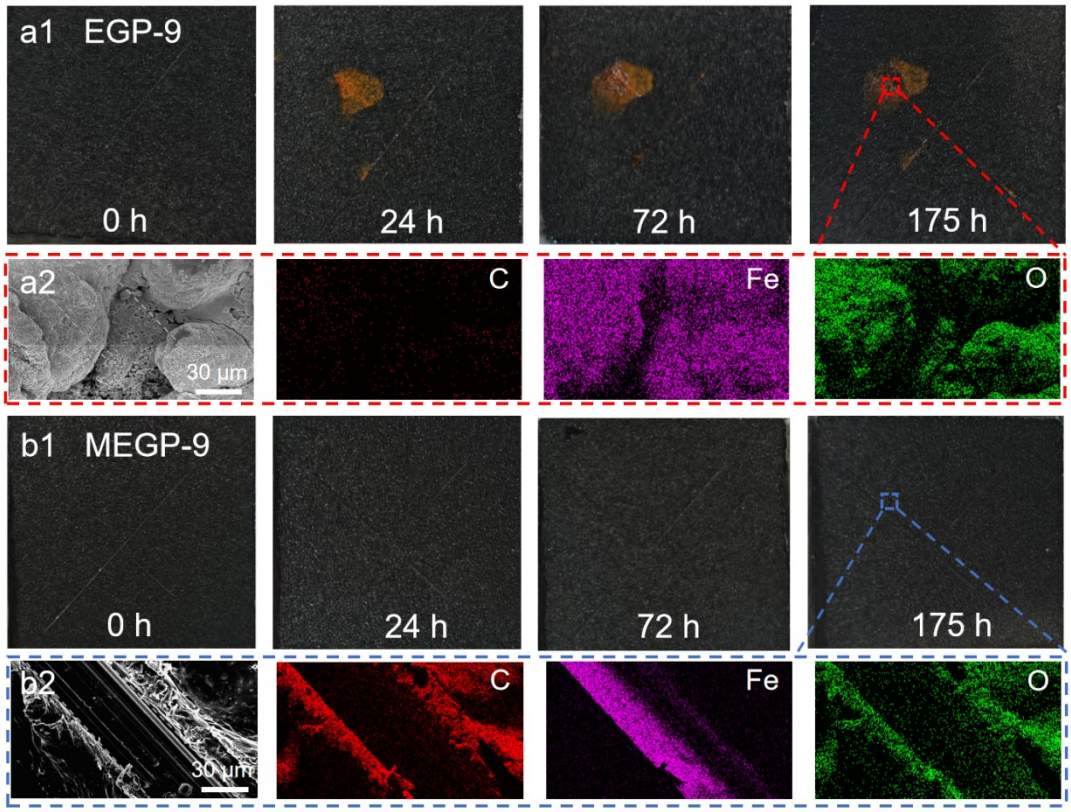

Fig. S17. The salt spray test of MEGP-9 and EGP-9 coatings. The digital image of EGP coating (a1) and MEGP coating (b1). The SEM image and EDS of EGP coating (a2) and MEGP coating (b2).

Salt spray test

To examine the corrosion resistance performance of scratched coatings, the coatings with artificial defects were exposed to a salt spray environment for 175 h. The test results for MEGP-9 coating and EGP-9 coating showed significant differences. After just 24 hours, yellow corrosion products were already visible at the scratch sites of the EGP-9 coating (**Fig. S17a1**), while there were no noticeable changes at the scratch sites of the MEGP-9 coating (**Fig. S17b1**). At the same time, as the salt spray test time is extended, the differences become increasingly apparent. To further observe the microscopic changes in the scratched area of the coating, we captured SEM images of the scratches. Test results showed that after 175 hours of salt

spray testing, scratches on the MEGP-9 coating are still clearly visible in SEM and EDS images, and there are no obvious iron corrosion products inside the scratches **(Fig. S17b2)**. In contrast, the scratches on the EGP-9 coating were completely covered by corrosion products, and EDS analysis detected a significant amount of iron corrosion products on the coating surface, indicating complete corrosion of the coating **(Fig. S17a2)**.

Table S1

Comparison of carbon-based high TC protective coatings with previous reports.

Coating name	TC, W m^{-1} K^{-1}	Infrared emissivity	$\|Z\|_{0.01Hz}$, Ohm cm^2	Impact resistance, cm	Adhesion strength, MPa	Years
epoxy/MrGO-6	0.7	-	10^8-10^9(11 d)	-	-	2022[11]
I-PDA-G-EP	$0.8_{//}$ $0.2_{\perp}$	-	3.0×10^9 (30 d)	-	-	2022[12]
tGNPs/tCNTs/ TSiPD	2.9	-	~ 10^3 (2 d)	>50 cm·kg	0 grade	2020[13]
rGO-BTA@HMS/epoxy	1.2	-	3.4×10^6 (35 d)	-	-	2024[14]
Gr/PFA	0.3	-	10^{11} (30 d)	-	-	2022[15]
EP-8	1.5	-	9.4×10^{10} ($\|Z\|_{0.8Hz}$, 30 d)	-	1 grade	2025[16]
SiO@GR/EPR	0.67	-	1.1×10^{11} (7 d)	-3.5	3.5	2025[17]
MEGP	**$2.6_{\perp}$**	**0.95-0.98**	**6.5×10^8 (90 d)**	**100**	**10.4**	**This work**

Notes: '-' indicates that the relevant property was not studied in the article.

References

1. H. Chen, V.V. Ginzburg, J. Yang, Y. Yang, W. Liu and Y. Huang, Thermal conductivity of polymer-based composites: Fundamentals and applications, *Prog. Polym. Sci.,* 2016, **59**, 41-85.
2. J. Li, F. Li, X. Zhao, W. Zhang, S. Li and Y. Lu, Jelly-inspired construction of the three-dimensional interconnected BN network for lightweight, thermally conductive, and electrically insulating rubber composites, *ACS Appl. Electron. Mater.,* 2020, **2**, 1661-1669.
3. M. Qin, Y. Xu, R. Cao, W. Feng and L. Chen, Efficiently controlling the 3D thermal conductivity of a polymer nanocomposite via a hyperelastic double-

continuous network of graphene and sponge, *Adv. Funct. Mater.,* 2018, **28**, 1805053.

4. C. Wu, S. Zhang, M. Liu and J. He, One-step solvothermal synthesis of nitrogen-doped carbon dots with efficient red emission from conjugated perylene for multiple applications, *Carbon,* 2024, **230**, 119601.
5. C. Zhu, Y. Fu, C. Liu, Y. Liu, L. Hu and J. Liu, Carbon dots as fillers inducing healing/self-healing and anticorrosion properties in polymers, *Adv. Mater.,* 2017, **29**, 1701399.
6. Y. Pang, J. Wei, Y. Wang and Y. Xia, Synergetic protective effect of the ultralight MWCNTs/NCQDs modified separator for highly stable lithium–sulfur batteries, *Adv. Energy Mater.,* 2018, **8**, 1702288.
7. A. Sarnecki, P. Adamski, A. Albrecht, A. Komorowska, M. Nadziejko and D. Moszyński, XPS study of cobalt-ceria catalysts for ammonia synthesis – The reduction process, *Vacuum,* 2018, **155**, 434-438.
8. F. Xu, P. Ye, J. Peng, H. Geng, Y. Cui and D. Bao, Cerium methacrylate assisted preparation of highly thermally conductive and anticorrosive multifunctional coatings for heat conduction metals protection, *Nano-Micro Lett.,* 2023, **15**, 201.
9. T. Xiao, L. Wang, K. Li, J. Tang, R. Du and S. Rao, Donor-acceptor-donor organic small molecules as hole transfer vehicle covalently coupled $Znln_2S_4$ nanosheets for efficient photocatalytic hydrogen evolution, *Adv. Funct. Mater.,* 2025, **35**, 2412644.
10. Q. Yue, Z. Zhang, X. Liu, C. Zhu, Y. Wen and P. Fu, Engineering electron delocalization of ultrathin covalent organic framework nanosheets to elevate photocatalytic hydrogen evolution in seawater, *Chem. Eng. J.,* 2025, **507**, 160481.
11. Z. Yang, S. Yu, W. Sun, Z. Xing, W. Gao and L. Wang, High-efficiency preparation of reduced graphene oxide by a two-step reduction method and its synergistic enhancement of thermally conductive and anticorrosive performance for epoxy coatings, *Ind. Eng. Chem. Res.,* 2022, **61**, 3044-3054.
12. J. Ding, H. Zhao and H. Yu, Bio-inspired multifunctional graphene–epoxy anticorrosion coatings by low-defect engineered graphene, *ACS Nano,* 2022, **16**, 710-720.
13. Q. Shi and A. Zhu, Interface regulation of graphene/carbon nanotube on the thermal conductivity and anticorrosion performance of their nanocomposite, *Prog. Org. Coat.,* 2020, **140**, 105480.
14. Z. Yang, J. Che, Z. Zhang, L. Yu, M. Hu and W. Sun, High-efficiency graphene/epoxy composite coatings with outstanding thermal conductive and anti-corrosion performance, *Compos. Pt. A-Appl. Sci. Manuf.,* 2024, **181**, 108152.
15. B. Li, K. Xu, W. Sun, L. Wang, Z. Yang and G. Liu, Beyond graphene: Anticorrosion performance of fluorographene-filled perfluoroalkoxy alkane composite coatings for condensing heat exchanges, *Prog. Org. Coat.,* 2022, **165**, 106748.

16. G. Ren, W. Zheng, Z. Qiao, Y. Tuo, X. Chen and Q. Zhao, Thermally conductive superhydrophobic composite coatings with anti-corrosion property, *Prog. Org. Coat.,* 2025, **198**, 108913.
17. W.-X. Ma, W.-W. Cong, L.-Y. Guo, J.-B. Wang, L. Cui and X. Sun, Preparation of thermally conductive and anti-corrosion coating by the insulation modification on graphite, *Ceram. Int.,* 2025, **51**, 2411-2419.